ABSTRACT

STEVENS, ELLIS JOHN. A Digital Sensorless BLDC Motor Control Algorithm Utilizing Line-to-Line Voltages for Aerospace Applications. (Under the direction of Dr. Gregory Buckner.)

This paper details the development of a digital rotor position estimation algorithm for BLDC motors utilizing line-to-line signals. Reducing the use of external sensors reduces cost and risk of failure in the motor. Current methods use electrical circuits for Zero Crossing Point (ZCP) detection, however this implementation can be retrofitted onto existing architecture without additional hardware changes. Experimental testing is performed using the algorithm on a 3-phase, 8 pole-pair BLDC motor embedded within a Circular Force Generator (CFG) using a industry standard microcontroller. The results are compared against a more conventional Hall sensing method. The testing confirms accurate velocity tracking to within a 1 RPM error and maintain consistent power consumption. Although the algorithm is proven to be effective in a laboratory setting, additional testing on aircraft vibration cancellation hardware is recommended to validate performance when dynamic loads are applied.

A Digital Sensorless BLDC Motor Control Algorithm Utilizing Line-to-Line Voltages for Aerospace Applications

by
Ellis John Stevens

A thesis submitted to the Graduate Faculty of
North Carolina State University
in partial fulfillment of the
requirements for the Degree of
Master of Science

Mechanical Engineering

Raleigh, North Carolina

2021

APPROVED BY:

Dr. Larry Silverberg

Dr. Andre Mazzoleni

Dr. Gregory Buckner
Chair of Advisory Committee

DEDICATION

To my friends and family for all their support.

BIOGRAPHY

The author was born in the North of England where he lived until moving to Charlotte, North Carolina at the age of 11. After receiving his International Baccalaureate diploma, he attended North Carolina State University where he achieved a Bachelors degree from the Mechanical and Aerospace Engineering Department. After working as an intern in the Electromechanical systems group at LORD coporation for 6 months, he began pursuing a Masters degree at North Carolina State University, focusing on motor control.

ACKNOWLEDGEMENTS

I would like to thank Greg Fricke, Anthony Hunter, Doug Swanson and Daniel Kakaley at LORD corporation for their help throughout the entire process. I would also like to thank my advisor for motivating me to reach my potential.

TABLE OF CONTENTS

LIST OF TABLES

LIST OF FIGURES

CHAPTER

1

INTRODUCTION

Significant advancements in recent decades to power electronics, permanent magnet (PM) technologies and microcontrollers have shifted the brushless DC (BLDC) motor from research and development laboratories to widespread commercial implementation in robotics, automation, process control and vehicle systems. Replacing the rotor windings and brushes found on conventionally commutated DC motors with energy-dense permanent magnets has eliminated issues related to brush wear, and has increased motor performance, efficiency and longevity [Sha03] [Pil91]. The BLDC motor is now commonly deployed in a variety of aerospace applications including electric propulsion systems, unmanned aerial vehicles, and NASA's Mars Curiosity Rover [Dah19] [Gab11] [Mah12]. Because there is no direct electrical connection to the BLDC rotor, fixed sensors and microcontrollers are implemented to provide rotor position feedback for the electrical commutation of stator phases.

Hall effect sensors, which provide voltages proportional to magnetic field intensity, are frequently used for BLDC commutation. Their compact size, simplicity and robustness make them well-suited for contactless rotor position sensing. By appropriately positioning Hall effect sensors inside the motor, their voltage gradients (caused by proximity to rotor PMs) can be used to accurately estimate rotor position. This technique has been applied to BLDC motors in numerous aerospace applications; one example is Circular Force Generators (CFGs) used in active vibration control systems. These devices rotate unbalanced masses at N/rev blade pass frequencies to produce forces or torques that are 180 degrees phase-shifted with respect to measured aircraft vibration [Swa15]. While the BLDC motors used to drive the unbalanced masses typically utilize Hall effect sensors for position sensing, there are potential benefits to reducing CFG size, weight, and cost while simultaneously enhancing performance by removing this sensing hardware [Kim07]. As such, an alternate

(but equally effective) means of rotor position feedback is required.

Sensorless control is an alternative strategy for BLDC motor commutation; this approach involves estimating rotor position in real-time based on stator back-EMF signals. It has the potential to increase reliability and robustness, and decrease cost, by reducing the number of parts subject to failure [Lin08]. Zero Crossing Points (ZCPs) in these back-EMFs can be identified and used to estimate rotor position using simple analog or digital hardware [Lin08] [Che18] [Fae09]. The relationship between back-EMFs and commutation signals is illustrated in Fig. 1.1; a 30 degree phase difference exists between the ZCPs and the commutation points. Published ZCP detection strategies reveal technical challenges which can result undesirable BLDC motor performance (excessive torque ripple, etc.) [Kim07] [Sha03] [Che05].

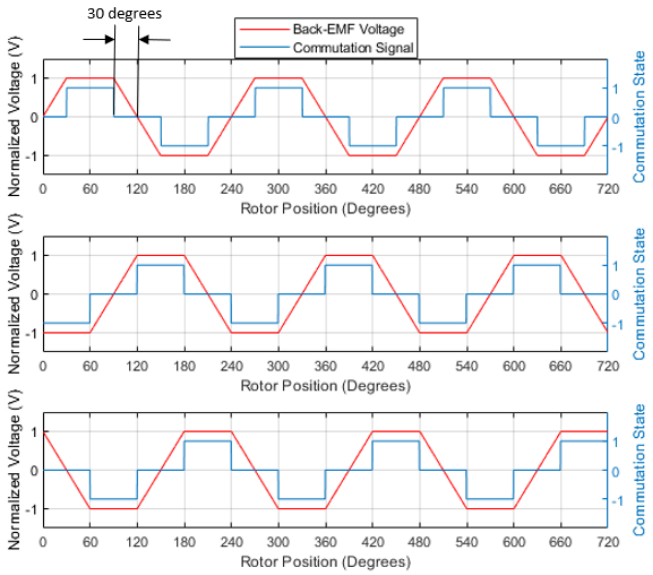

Figure 1.1 Stator back-EMF voltages (red) and commutation signals (blue) for phases: A (top), B (middle), and C (bottom), plotted as functions of rotor position. The ZCPs on the back-EMF signals occur 30-degrees prior to changes in commutation state.

One such challenge involves a non-static virtual neutral: the intersection of the motor phases located at the center of the motor windings which measures the average of all motor phase voltages. High harmonic noise is exhibited on the virtual neutral point due to Pulse Width Modulation (PWM) of phase voltages [Sha03]. Non-static virtual neutrals cause back-EMF voltages to fluctuate, which causes variations in ZCP detection increase, resulting in improperly timed commutation sequences. Some researchers are investigating sliding mode observers and extended Kalman filters to remedy these limitations [Ejl12] [Ais16] [Mur18], though simpler solutions such as analog low-pass filters have been used [Kim07]. These sensorless ZCP detection methods do not completely address the issue of limited available space for certain aerospace applications, as they require additional circuitry.

Replacing terminal voltage signals with line voltage measurements has been proposed by Li, et al. [Li13] as a means of reducing position error through using a more stable reference than the virtual neutral point, which reduces variations in commutation timings and produces less torque ripple [Che05]. Fig. 1.2 illustrates the difference between a terminal voltage and a line voltage. Additionally, ZCPs detected using line-to-line voltages (that is, the line voltage of one phase subtracted from the line voltage of a neighboring phase) coincide directly with commutation instances. This allows commutations to occur directly proceeding a ZCP detection, eliminating the need for phase delay circuitry and thus reducing circuit complexity [Lad13].

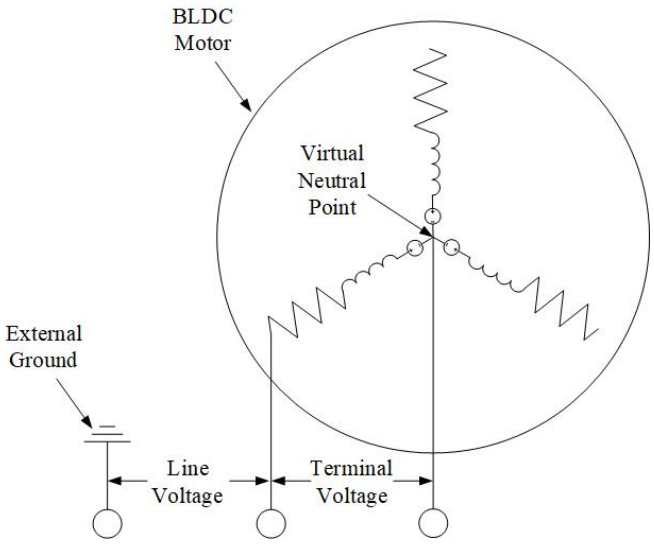

Figure 1.2 Electrical Schematic of a BLDC motor contrasting line voltage and terminal voltage measurements. Terminal voltages are measured with reference to the virtual neutral point, the average voltage across all motor phases. Line voltages are measured with reference to an external ground, a more stable reference than the virtual neutral.

Applying the aforementioned voltage signals to the ZCP detecting methods outlined above has allowed researchers to construct cheaper and more robust sensorless control algorithms [Lad13]. However, BLDC tracking performance remains limited by the availability of position feedback generated solely from ZCP detection. Though line-to-line voltage position sensing techniques have been presented in previous works, there does not presently exist a method for position estimation between sector crossings which can provide controllers with continuous feedback.

This paper presents an experimentally-validated sensorless motor control algorithm which utilizes line-to-line voltages to provide complete position information. A discrete time derivation of electrical and mechanical position and from ZCPs detected on line-to-line voltages is discussed. The algorithm is then implemented on a 3-phase, 8 pole-pair BLDC motor embedded within a CFG and commutated using trapezoidal waveforms. Performance is experimentally verified through experimental comparisons against more conventional Hall effect commutation methods.

To ensure the algorithm is suitable for a range of applications, velocity tracking error and power consumption performance are evaluated at steady-state and ramped velocity setpoints using the sensorless algorithm and traditional Hall effect sensing. Unlike existing sensorless control strategies, this algorithm can be retroactively integrated onto existing BLDC architectures without additional hardware, and can efficiently run at a 10 kHz loop rate on industry standard microcontrollers.

CHAPTER

2

METHODS

2.1 Derivation

ZCPs are detected based on +/- sign changes in the line-to-line voltages: V_{ab}, V_{bc}, V_{ca}. Fig. 2.1a illustrates the relationships between these line-to-line voltages and identifies ZCPs as functions of electrical angle ϕ. These voltages are computed based on stator line voltages, V_a, V_b, V_c, which are measured with respect to an external ground.

$$\begin{bmatrix} V_{ab} \\ V_{bc} \\ V_{ca} \end{bmatrix} = \begin{bmatrix} 1 & -1 & 0 \\ 0 & 1 & -1 \\ -1 & 0 & 1 \end{bmatrix} \begin{bmatrix} V_a \\ V_b \\ V_c \end{bmatrix} \tag{2.1}$$

Prior to analog-to-digital conversion, these stator phase voltages are filtered using a first-order low-pass filter with a 5 kHz cutoff frequency, the approximate Nyquist frequency of the 10 kHz acquisition rate, for anti-aliasing.

Sign changes are detected by multiplying the current and previous line-to-line voltages: $V_{xy}[k] \cdot V_{xy}[k-1]$; a negative product indicates that a zero crossing has occurred. Once a ZCP is detected, a look-up table uses the +/- signs of other line-to-line voltages to evaluate the present rotor sector position λ, as detailed in Table 2.1. Rotor position can be estimated assuming a constant rotor angular velocity between ZCPs:

$$\phi[k] = \phi_\lambda[m] + (\omega[m] N[k] D[m]) T_s^{-1}, \tag{2.2}$$

where $\phi[k]$ is the present electrical angle, $\phi_\lambda[m]$ is the electrical angle associated with the present

sector m, $\omega[m]$ is the estimated average rotor angular velocity, $N[k]$ is the present clock count, and $D[m]$ is the direction factor. Both $\Phi[k]$ and $N[k]$ operate at the processor time step k, whereas $\phi_\lambda[m]$, $\omega[m]$, and $D[m]$ are calculated following each ZCP detection, m. T_s denotes the acquisition rate. Fig. 2.2 presents a block diagram illustrating the algorithm calculations with reference to their

Table 2.1 Relationships between ZCPs on stator phases, sector position, and electrical angle

V_{ab}	V_{bc}	V_{ca}	Sector Position λ	Electrical Angle ϕ_λ
ZCP	+	-	4	180
ZCP	-	+	1	0
+	ZCP	-	3	120
-	ZCP	+	6	300
+	-	ZCP	2	60
-	+	ZCP	5	240

relative sample rates. To determine the direction factor, the difference in sector position is evaluated. A difference of +1 or -5 denotes a counter clockwise (CW) rotation as referenced in Fig. 2.1b, while a difference of -1 or +5 denotes a counter clockwise (CCW) rotation:

$$D[m] = \begin{cases} 1, & \lambda[m]-\lambda[m-1] = 1,-5 \\ -1, & \lambda[m]-\lambda[m-1] = -1,5 \end{cases}, \tag{2.3}$$

Average rotor angular velocity is calculated using:

$$\omega[m] = \frac{\Delta\theta}{\Delta t}, \tag{2.4}$$

where $\Delta\theta$ represents the rotor's angular displacement (in electrical degrees) over a discrete interval of time Δt. Since the displacement is only detected at sector crossings, $\Delta\theta$ equals the length of a sector: 60 degrees. The time interval Δt is thus defined as the elapsed time between successive ZCP detections:

$$\Delta t = t[m]-t[m-1] = ((N[m]+f[m])-(N[m-1]+f[m-1])Ts^{-1}. \tag{2.5}$$

Here $t[m]$ and $t[m-1]$ represent the time at the m^{th} and $(m-1)^{th}$ ZCP, respectively, f is the fractional count between the ZCP and the clock count preceding it, and Ts^{-1} is the inverse sample rate of the processor. Fig. 2.3 illustrates how line-to-line voltages V_{ab} and V_{bc} are sampled.

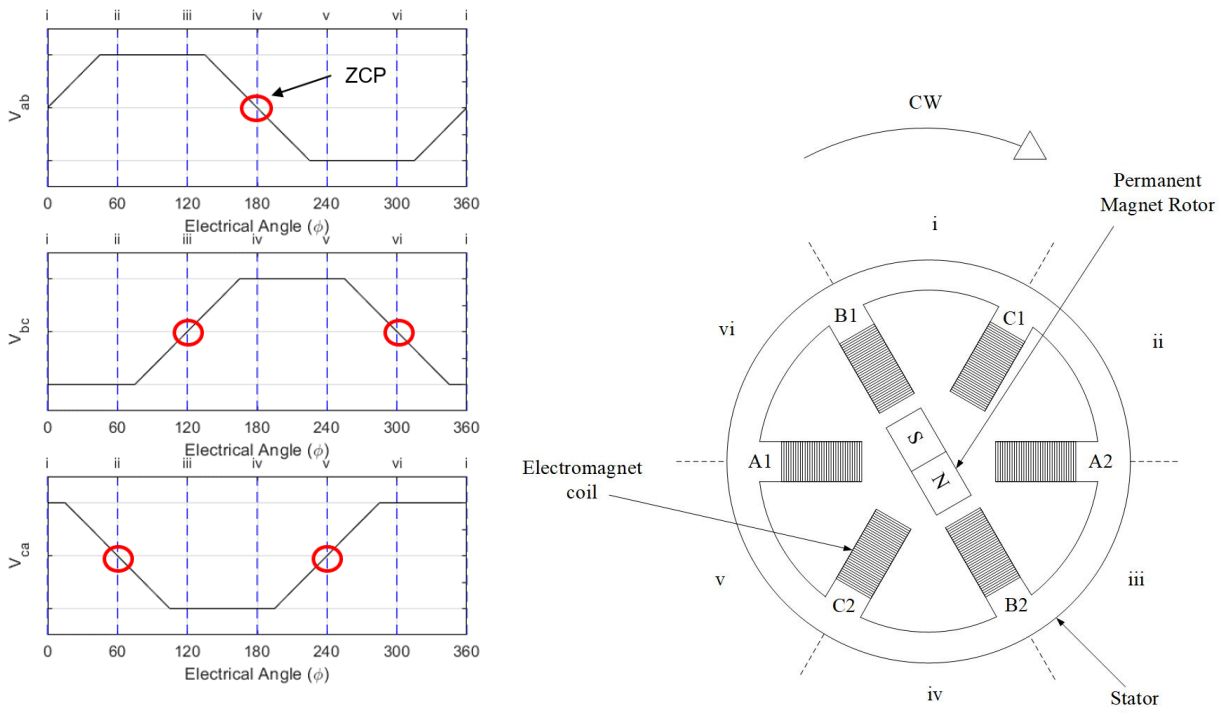

(a) **(b)**

Figure 2.1 a) Normalized line voltage differences V_{ab}, V_{bc} and V_{ca} plotted as functions of electrical angle ϕ. Red circles indicate the location of ZCPs with dashes lines showing the sector crossings. The rotor position associated with each sector crossing on a 3-phase, 2-pole BLDC motor is shown in b).

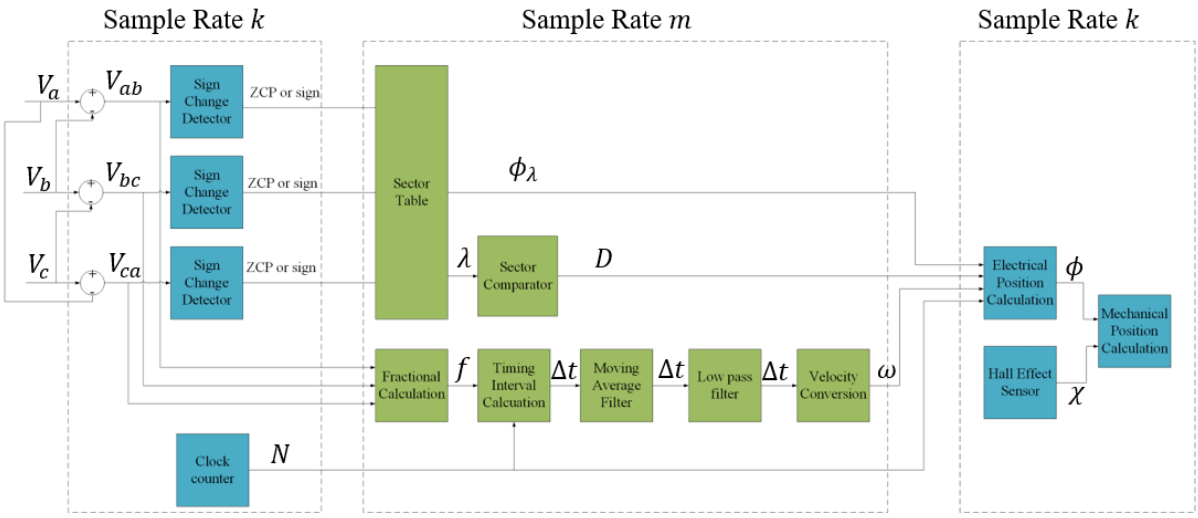

Figure 2.2 Block diagram detailing the calculations performed by the algorithm. Blocks highlighted in blue operate at the microprocessor sample rate k, whereas those highlighted in green are only calculated following a ZCP detection, denoted by the sample rate m. The latter sample rate varies with rotor velocity.

Fractional clock counts are estimated based on a linear relationship close to the x-axis:

$$f = \frac{(V[k-1])}{(V[k-1]-V[k])}. \tag{2.6}$$

By resetting the clock count to 1 after a ZCP detection, $N[m-1]$ is eliminated from Eq. 2.5, resulting in:

$$\Delta t = t[m]-t[m-1] = (N[m]+f[m]-f[m-1])Ts^{-1}. \tag{2.7}$$

The timing interval calculation in Eq. 2.7 exhibits amplitude distortion artifacts caused by variations in pole placement. To overcome these distortions, a digital fifth-order Finite Impulse Response (FIR) filter is applied to the timing calculations. Additionally, using a digital second-order Butterworth filter with a cutoff frequency equal to the rotational speed of the motor, once-per-rev amplitude distortions caused by gravitational effects on the motor's load are mitigated. Since the sample rate of timing interval calculations is dependent on motor speed, a static cutoff frequency would produce different responses at different motor speeds. Magnitude response plots for both filters are shown in Fig. 2.4.

When determining commutation sequences, typical BLDC motor applications attempt to minimize electrical and mechanical rotor position error through the use of a PI controller. As such a derivation of mechanical position is required. Mechanical rotor position θ is calculated as:

$$\theta[k] = (\phi[k]+\chi[k])P^{-1} = (\phi_\lambda[m]+(\omega[m]N[k]D[m])T_s^{-1}+\chi[k])P^{-1}, \tag{2.8}$$

where P is the pole pair number and $\chi[k]$ is a scalar variable incremented by 1 following each electrical cycle. Upon detecting the trailing edge of a Hall effect sensor voltage placed at the motors' mechanical position origin, $\chi[k]$ is reset to 0.

2.1.1 Experimental Setup

The sensorless control algorithm was evaluated experimentally using a 3-phase, 8 pole-pair BLDC motor embedded within a CFG. The motor's architecture and the microcontroller were treated as an isolated system for these experiments; other CFG internal components were not utilized.

As shown in Fig. 2.5, two Xantrex XHR 300-3.5 DC power supplies were connected to the motor's inverter terminals, acting as the +/- 135 V rail. The Texas Instruments C2000 microcontroller connected to the motor's inverter received power from a 28 V Soresen XG 100-8.5 power supply. A Probe Master 4231 voltage sensor was connected to the +/- 135 V rails in parallel to the motor's inverter to measure DC voltages. A Tetronix A622 inductive current sensor was clamped around the + 135 V rail prior to the motor's inverter. Analog voltage and current data were acquired by these devices and converted to digital TDMS files by a National Instruments NI-9174 Data Acquisition Chassis using a 10 kHz NI-91239 Analog Input Card. Data was then transmitted via a serial interface to a desktop computer for post-processing. These measurements were used to calculate power consumption throughout motor performance using the equation $P = IV$.

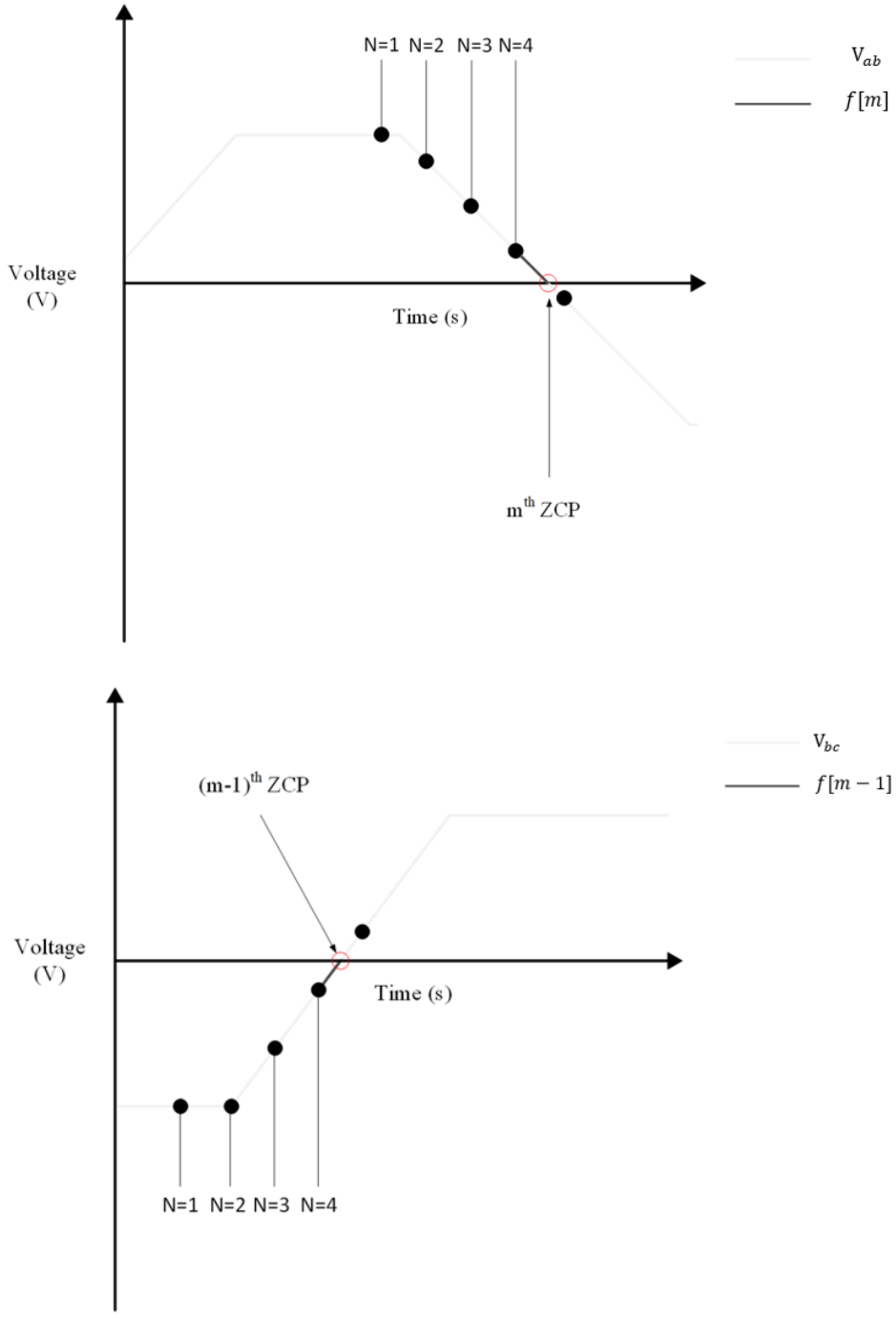

+

Figure 2.3 Timing intervals between ZCPs (highlighted by red circles) illustrated as a function of whole and fractional clock counts. Discrete samples of back EMF signals are illustrated with corresponding clock count values. Fractional clock counts are highlighted in dark grey.

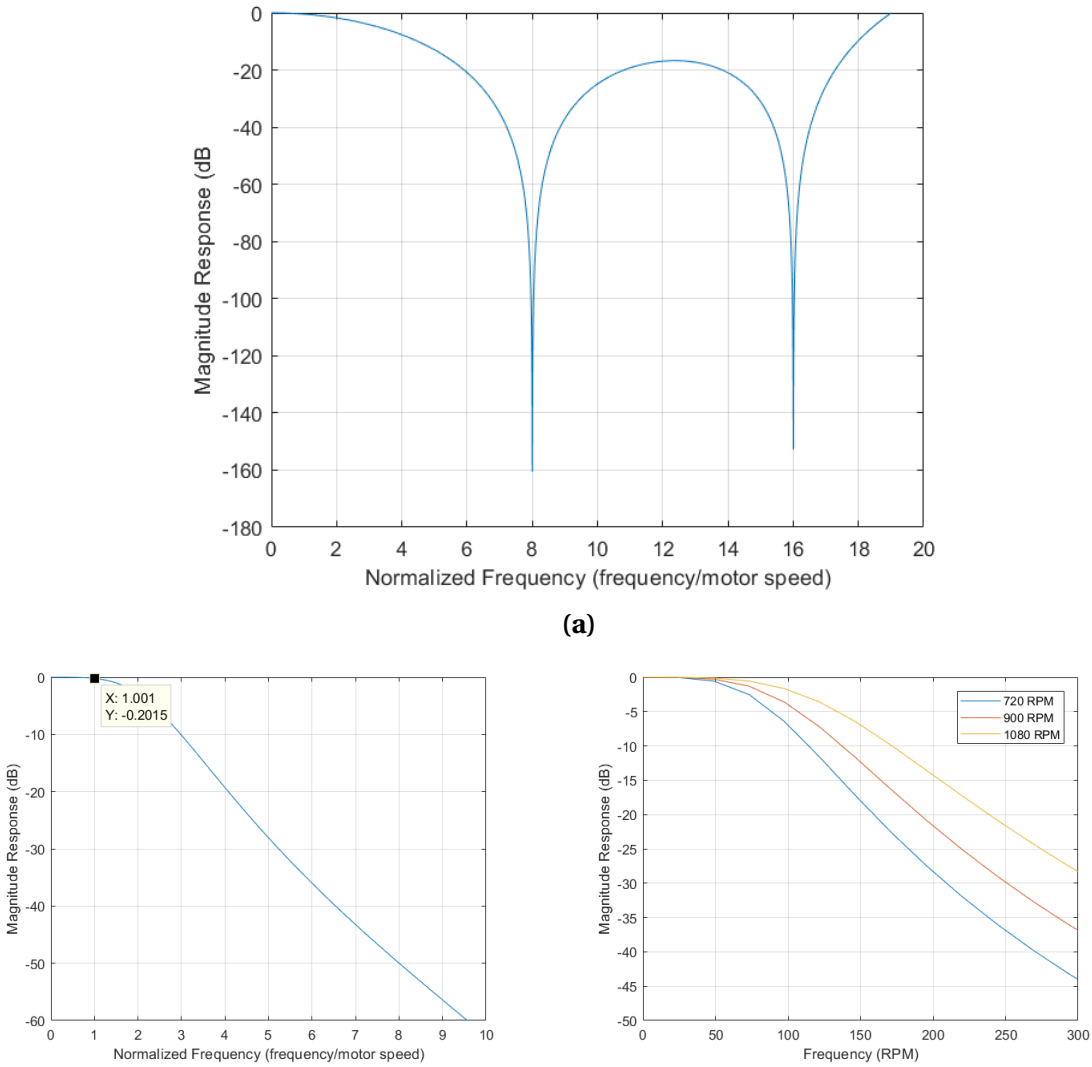

Figure 2.4 Magnitude response graphs to the a) digital fifth-order FIR filter, b) normalized digital second-order low-pass filter and c) 3 digital second-order low-pass filters with the same cutoff frequency but different motor speeds.

Table 2.2 Table of equipment used in experimental setup

Description	Manufacturer	Model Number
Power Supply 135VDC	Xantrex	XHR 300-3.5
Power Supply 28VDC	Sorensen	XG 100-8.5
Voltage Sensor	Probe Master	4231
Inductive Current Sensor	Tetronix	A622
Data Acquisition Chassis	National Instruments	NI-9174
Analog Input Card	National Instruments	NI-9239
Microcontroller	Texas Instruments	C2000
CAN to USB Converter	National Instruments	NI-XNET-8502/2
Computer	Dell	Dell Precision M4800

The algorithm was programmed using Simulink 2012a a software package for MATLAB. Standalone C code was then auto-generated from the Simulink model, using the MATLAB Coder add-on, and compiled into an embedded application hex file. A bootloader software, C2Prog loader, programmed the hex file through a Controller Area Network (CAN) terminal bus using the CAN Calibration Protocol (CCP). A National Instruments NI-XNET-8502/2 CAN to USB converter connected between the computer and microcontroller allowed the CAN messages to be transmitted. A list of equipment used in the experimental setup can be found in Table 2.2.

Line voltages, measured with respect to the motor's chassis, were filtered using the first order analog low-pass filter with a 5kHz cutoff frequency, digitally acquired and passed to the microcontroller for processing via the sensorless algorithm. The PI controller outlined in Fig. 2.6 was implemented using a heuristic tuning method to minimize velocity tracking error and power consumption.

To determine the algorithm's estimation accuracy and its effect on motor efficiency, steady-state and ramped velocity changes were applied to the motor within a range of velocities typically utilized for high speed BLDC motor aerospace applications. Angular velocity, current and voltage data were measured throughout each test. Hall effect sensors placed at each pole location within the motor were utilized for verification purposes. Timing differences between trailing edge detection between sensors were converted to velocity using Eq. 2.4.

Angular velocity data from both measurement methods were saved via embedded software to static memory locations on the microcontroller and retrieved via a CAN terminal bus using the CCP at a 10 kHz sample rate. During the motor startup procedure, Hall effect sensors were initially used for position sensing until a line voltage magnitude threshold of 80 V was detected by the microcontroller on all phases, at which point the motor used the sensorless algorithm.

To quantify and compare the algorithm's effect on motor efficiency, Hall effect sensors were used for position sensing for the same velocity profiles, while current and voltage measurements were recorded. Power consumption was then calculated using $P = IV$.

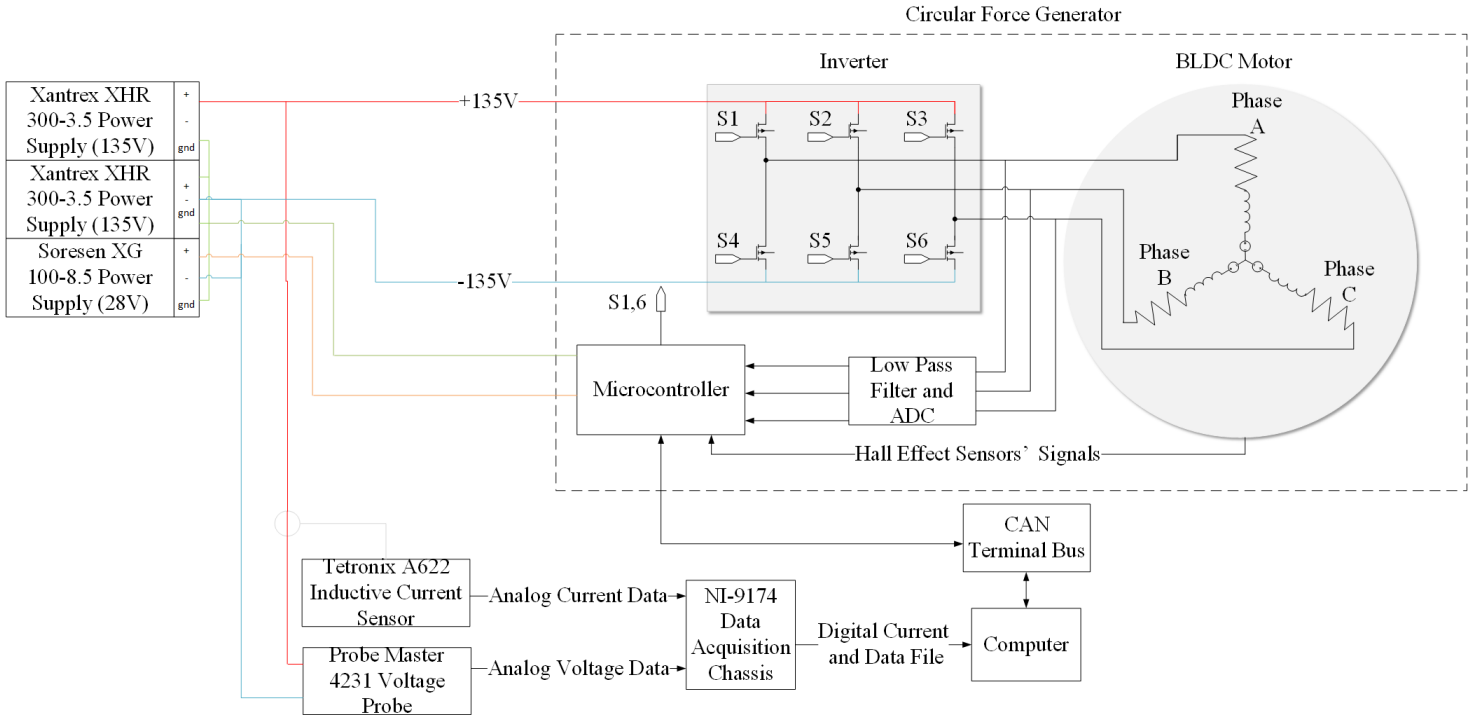

Figure 2.5 Block diagram of the setup used for experimental verification, highlighting the power distribution and control of the motor, and the data acquisition hardware. Both the sensorless algorithm commutation method and the Hall effect commutation method were examined using this setup.

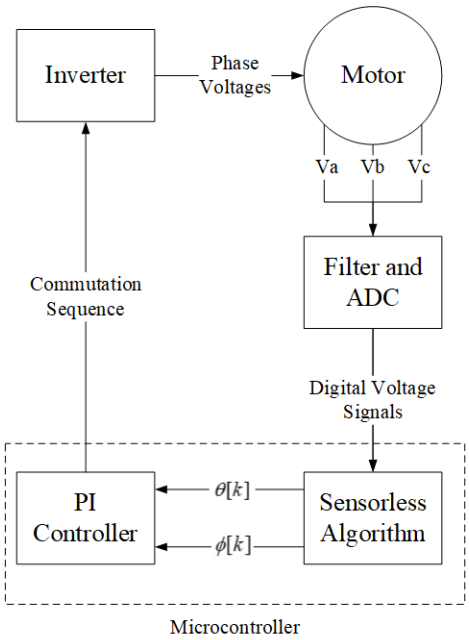

Figure 2.6 Microcontroller interaction with the BLDC motor. Analog voltage signals are digitally acquired for processing via the sensorless algorithm. Electrical and mechanical position estimates are passed to the PI controller, which determines the commutation sequences used by the inverter to drive the motor.

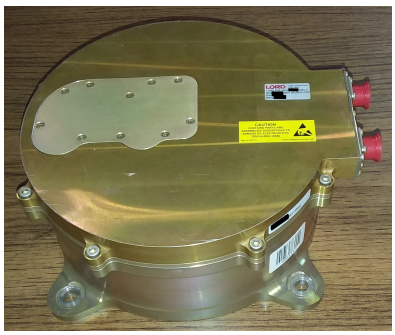

(a)

(b)

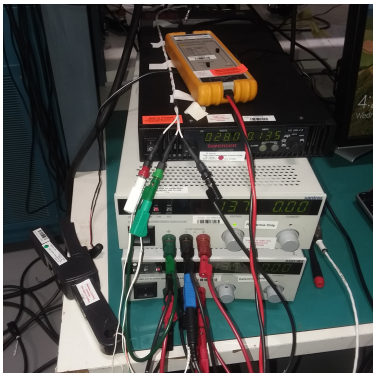

(c)

Figure 2.7 Photos of the test setup.
a) CFG with the 3-phase, 8 pole-pair BLDC motor and micontroller.
b) National Instruments DAQ Chassis containing the National Instruments Analog Input Card.
c) Xantrex and Sorensen power supplies with Probe Master voltage sensor on top and Tetronix current sensor clamped around the + 135 V rail as outlined in Fig. 2.5.

CHAPTER

3

RESULTS

Fig. 3.1 shows the velocity tracking accuracy of the sensorless algorithm. Three steady-state velocities common to aerospace applications were tested: 720, 900 and 1080 RPM. Both positive and negative ramped velocity setpoints were applied to the motor at a 180 RPM/s rate. Rotor velocity was measured by the sensorless algorithm and the Hall effect sensors; the error was calculated as:

$$\epsilon = \omega_E - \omega_{Measured}, \tag{3.1}$$

where ω_E is the rotor velocity measured by the sensorless algorithm and $\omega_{Measured}$ is the rotor velocity measured by the Hall effect sensors.

Table 3.1 Summary of velocity tracking results

Rotor Velocity (RPM)	ϵ (RPM)	$\lvert\epsilon\rvert$ (RPM)	$\lvert\epsilon\rvert$ (% of Velocity)	σ (RPM)
720	0.1877	0.2401	0.0333	0.2250
900	0.2966	0.3319	0.0368	0.2619
1080	0.2924	0.4190	0.0388	0.4187
720-900	0.3689	0.6850	0.0951	0.8098
900-1080	0.3689	0.7795	0.0866	0.9345
1080-900	0.2980	0.5752	0.0639	0.6977
900-720	0.1922	0.5463	0.0773	0.7010

Table 3.1 provides averages across each velocity region from Fig. 3.1 including error, error magnitude, error as a percentage of measured velocity, and standard deviation. The mean magnitude and the standard deviation in error increased with steady-state velocity, from 0.2401 RPM to 0.4190 RPM and 0.2250 RPM to 0.4187 RPM, respectively. Mean error percentage at steady-state remained consistently within a 0.03% to 0.04% range. Larger velocity tracking error magnitudes can be seen during ramped velocity changes, with positive acceleration changes exhibiting more error than negative changes. Mean tracking error magnitude reached a maximum between 900 RPM and 1080 RPM at 0.7795 RPM. Average error as a percentage of the measured velocity was between 0.08% to 0.1% during positive ramp changes and 0.06% to 0.08% during negative ramp changes.

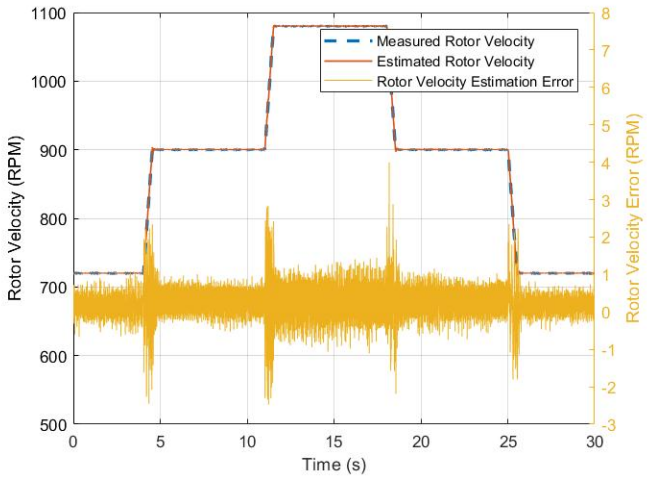

Figure 3.1 Plot of estimated rotor velocity via the sensorless algorithm and measured rotor velocity via the Hall effect sensors over a range of stepped velocities. Error between the two is plotted on the right axis. Error magnitude increases with rotor velocity but remains below 1RPM.

As shown in Fig. 3.2a, power consumption was measured for both commutation methods, using the sensorless algorithm and using Hall effect sensors, during the same velocity setpoint path as in Fig. 3.1. High frequency noise in the power data made differences in the two difficult to quantify. Fast Fourier Transforms (FFTs) of each data set (shown in Fig. 3.3) revealed high frequency noise occurring at 720 Hz on the Hall effect sensor commutation data and at 360 Hz on the sensorless algorithm commutation data. A second-order digital low-pass filter was applied with a cutoff frequency of 36 Hz was applied to the data. The cutoff frequency was chosen to be one decade below the desired -2 dB attentuation frequency. The filtered power consumption data is presented in Fig. 3.4. Mean and standard deviations of power consumption calculated at both steady-state velocity and ramped velocity changes for each rotor position sensing method can be found in Table 3.2 and Fig. 3.4. The largest difference in mean power consumption between the two methods occurred between 900 RPM and 1080 RPM where the sensorless algorithm used 1.58% more of the motors maximum rated power of the motor than was used by the Hall effect sensors.

Table 3.2 Summary of power consumption results

Rotor Velocity (RPM)	Mean Power: Hall (%)	Mean Power: Sensorless (%)	σ: Hall (%)	σ: Sensorless (%)
720	8.63	8.80	1.87	1.64
900	10.58	11.45	2.65	2.67
1080	13.79	13.94	3.51	3.65
720-900	13.19	13.09	3.43	3.16
900-1080	17.43	19.01	4.51	4.90
1080-900	8.26	8.99	2.29	2.72
900-720	8.41	8.13	2.16	1.76

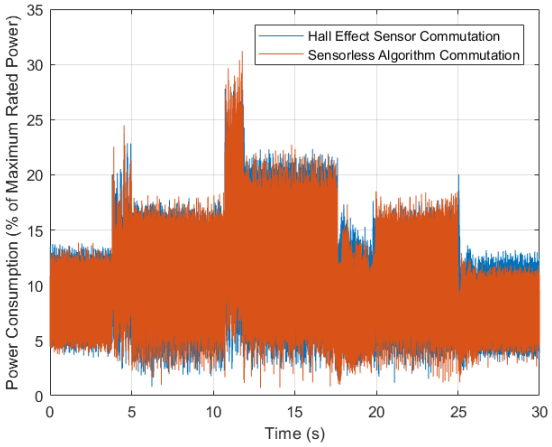

(a)

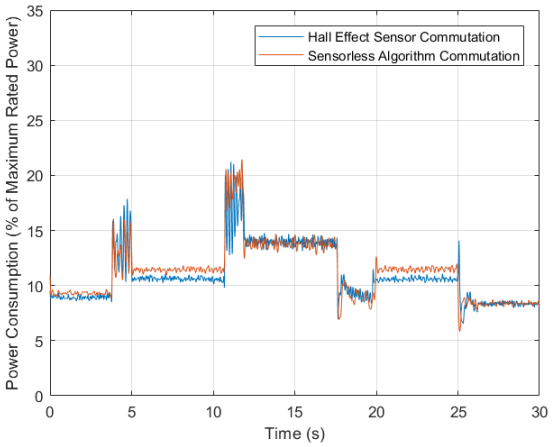

(b)

Figure 3.2 a) Pre-filtered power consumption data using the sensorless algorithm vs. Hall effect sensors as the position sensor plotted.
b) Post-filtered power consumption for the sensorless algorithm as the rotor position sensor and whilst using the Hall effect sensors as the position sensor.

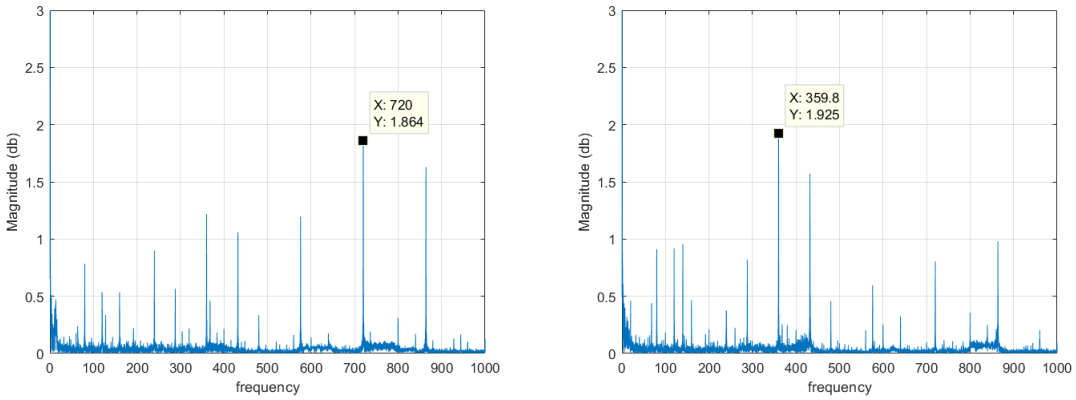

(a) **(b)**

Figure 3.3 Fast Fourier Transforms of velocity data for the a) measured rotor velocity, and b) estimated rotor velocity, respectively. High frequency noise occurs at 720 Hz and 360 Hz for measured rotor velocity, and estimated rotor velocity, respectively.

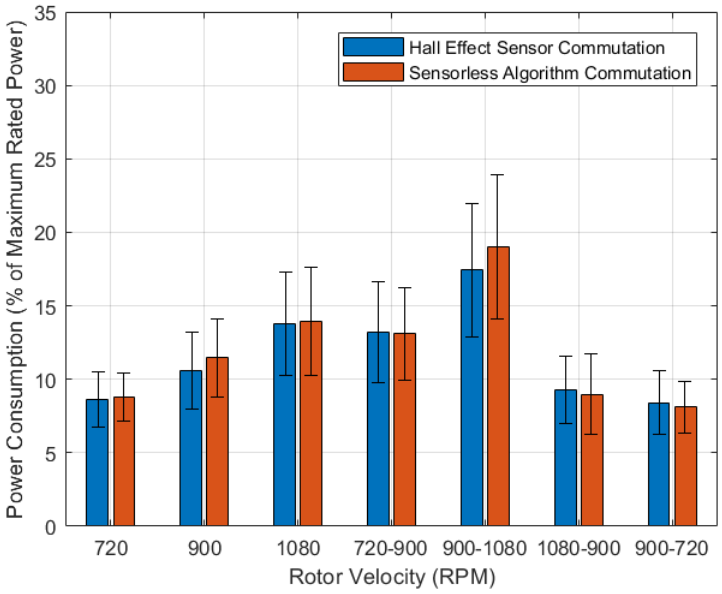

Figure 3.4 A bar graph summarizing the data of Table 3.2. The error bar magnitudes represent standard deviations in the pre-filtered power consumption data. The maximum power consumption for the sensorless algorithm was 1.58% higher than that of Hall effect sensing

CHAPTER

4

DISCUSSION

As demonstrated in Fig. 3.1, the sensorless algorithm proved capable of precisely tracking steady state velocities with an error below 1 RPM. This error magnitude increased during ramped setpoint changes, though the maximum error magnitude, 0.78 RPM, is sufficiently small for typical BLDC applications. It is clear from Fig. 3.1 that the sensorless algorithm was more accurate at tracking velocities during ramped negative acceleration than during positive acceleration. This was likely due to the algorithm extrapolating forward the linear velocity calculated from the previous sector crossing to determine the present sector position. This underestimated the position during positive acceleration, resulting in overcompensation from the controlle. Improvements to the tracking performance during ramped velocity changes could be made by adjusting the controller parameters using more traditional tuning methods, such as Zeigler-Nichols methods. Additionally, a higher-order position estimation model, such as assuming a square relationship to velocity, could be used to reduce tracking error.

Fig. 3.4 demonstrates that the sensorless algorithm maintained a similar power consumption (as compared to Hall effect position sensing) during both steady state velocity and velocity transitions. The experimental results shown in Table 3.2 indicate that differences in mean power consumption fluctuated as steady state velocity increased. However, the difference in standard deviation in power consumption changed from -0.61% at 720 RPM to 0.27% at 1080 RPM. At higher velocities, the sensorless estimation is more sensitive to the linear approximation of the line-to-line voltages around the ZCP, and is thus more sensitive to electrical noise. As a result, the algorithm's power consumption became more apparent as rotor velocity increased. These issues could potentially be reduced by using the same microcontroller to measure the velocity from both the sensorless algorithm and the Hall effect sensors. Alternating measurements were taken during the experimental

comparison, resulting in an effective 5 kHz sample rate with no interpolation between values. As such, velocity measurements were not calculated at the same moment, but instead with a slight delay which could have injected some error into the experimental results.

This experimental validation shows that a software sensorless algorithm solution with no additional hardware constraints can efficiently used to commutate a BLDC motor both at steady state velocities and during positive and negative accelerations. The algorithm can accurately estimate rotor position using an industry standard microcontroller, though a microcontroller with a faster clock speed would further reduce estimation errors and power consumption variation. These tests benefited from no dynamic loads on the motor, however flight testing would be required to verify suitability in aerospace applications.

CHAPTER

5

CONCLUSION

A sensorless rotor position estimation algorithm for BLDC motors was developed using line-to-line signals. The algorithm was implemented onto an industry standard C2000 microprocessor with no additional hardware requirements, other than those already found on BLDC motor architectures. The performance of this algorithm was demonstrated experimentally on a 3-phase, 8 pole-pair BLDC motor and compared to Hall effect sensors placed on the motor. Experimental results confirm that the algorithm can track rotor velocity to a 1 RPM error and maintain consistent power consumption compared to more traditional position sensing method. Further improvements can be made with faster clock speed microcontrollers, and more sophisticated controller tuning methods such as Zeigler-Nichols. Additional testing on aircraft vibration cancellation hardware is recommended to verify performance in non-static reference frames.

BIBLIOGRAPHY

[Ais16] Aishwarya, V. & Jayanand, B. "Estimation and control of sensorless brushless DC motor drive using Extended Kalman Filter". *2016 International Conference on Circuit, Power and Computing Technologies (ICCPCT)* (2016), pp. 1–7.

[Che05] Chen, C. & Cheng, M. "A New Sensorless Control Scheme for Brushless DC Motors without Phase Shift Circuit". *2005 International Conference on Power Electronics and Drives Systems* **2** (2005), pp. 1084–1089.

[Che18] Chen, S. et al. "Adaptive Commutation Error Compensation Strategy Based on a Flux Linkage Function for Sensorless Brushless DC Motor Drives in a Wide Speed Range". *IEEE Transactions on Power Electronics* **33**.5 (2018), pp. 3752–3764.

[Dah19] Dahbi, M. & Doubabi, S. "Performance evaluation of electric vehicle brushless direct current motor with a novel high-performance control strategy with experimental implementation". *SAGE Journals* (2019).

[Ejl12] Ejlali, A. & Soleimani, J. "Sensorless vector control of 3-phase BLDC motor using a novel Extended Kalman". *2012 International Conference on Advances in Power Conversion and Energy Technologies (APCET)* (2012), pp. 1–6.

[Fae09] Faeq, M. & Ishak, D. "A new scheme sensorless control of BLDC motor using software PLL and third harmonic back-emf". *2009 IEEE Symposium on Industrial Electronics Applications* **2** (2009), pp. 861–865.

[Gab11] Gabriel, D. L. et al. "Brushless DC motor characterisation and selection for a fixed wing UAV". *IEEE Africon* (2011), pp. 1–6.

[Kim07] Kim, T. et al. "Position sensorless brushless DC motor/generator drives: review and future trends". *IET Electric Power Applications* **1**.4 (2007), pp. 557–564.

[Lad13] Lad, C. K. & Chudamani, R. "Sensorless brushless DC motor drive based on commutation instants derived from the line voltages and line voltage differences". *2013 Annual IEEE India Conference (INDICON)* (2013), pp. 1–5.

[Li13] Li, B. et al. "A new sensorless control method for brushless permanent magnet DC motors". *2013 IEEE International Symposium on Sensorless Control for Electrical Drives and Predictive Control of Electrical Drives and Power Electronics (SLED/PRECEDE)* (2013), pp. 1–7.

[Lin08] Lin, C. et al. "Position Sensorless Control for Four-Switch Three-Phase Brushless DC Motor Drives". *IEEE Transactions on Power Electronics* **23**.1 (2008), pp. 438–444.

[Mah12] Mahaffy, P. et al. "The Sample Analysis at Mars Investigation and Instrument Suite". *Space Science Reviews* **170**.1-4 (2012), pp. 401–478.

[Mur18] Murali, S. B. & Rao, P. M. “Adaptive sliding mode control of BLDC motor using cuckoo search algorithm”. *2018 2nd International Conference on Inventive Systems and Control (ICISC)* (2018), pp. 989–993.

[Pil91] Pillay, P. & Krishnan, R. “Application characteristics of permanent magnet synchronous and brushless DC motors for servo drives”. *IEEE Transactions on Industry Applications* **27**.5 (1991), pp. 986–996.

[Sha03] Shao, J. et al. “A novel microcontroller-based sensorless brushless DC (BLDC) motor drive for automotive fuel pumps”. *IEEE Transactions on Industry Applications* **39**.6 (2003), pp. 1734–1740.

[Swa15] Swanson, D. et al. “Active Vibration Control Using Circular Force Generators” (2015).